

ACCEPTED TO APJ: January 10, 2011

**The Gemini NICI Planet-Finding Campaign:
Discovery of a Substellar L Dwarf Companion to the
Nearby Young M Dwarf CD-35 2722¹**

Zahed Wahhaj¹, Michael C. Liu¹, Beth A. Biller¹, Fraser Clarke², Eric L. Nielsen³, Laird M. Close³, Thomas L. Hayward⁴, Eric E. Mamajek⁵, Michael Cushing⁶, Trent Dupuy¹, Matthias Tecza², Niranjan Thatte², Mark Chun¹, Christ Ftaclas¹, Markus Hartung⁴, I. Neill Reid⁷, Evgenya L. Shkolnik⁸, Silvia H. P. Alencar⁹, Paweł Artymowicz¹⁰, Alan Boss⁸, Elisabethe de Gouveia Dal Pino¹¹, Jane Gregorio-Hetem¹¹, Shigeru Ida¹², Marc Kuchner¹³, Douglas N. C. Lin¹⁴ and Douglas W. Toomey¹⁵

¹Based on observations obtained at the Gemini Observatory, which is operated by the Association of Universities for Research in Astronomy, Inc., under a cooperative agreement with the NSF on behalf of the Gemini partnership: the National Science Foundation (United States), the Science and Technology Facilities Council (United Kingdom), the National Research Council (Canada), CONICYT (Chile), the Australian Research Council (Australia), Ministério da Ciência e Tecnologia (Brazil) and Ministerio de Ciencia, Tecnología e Innovación Productiva (Argentina).

ABSTRACT

We present the discovery of a wide (67 AU) substellar companion to the nearby (21 pc) young solar-metallicity M1 dwarf CD–35 2722, a member of the \approx 100 Myr AB Doradus association. Two epochs of astrometry from the NICI Planet-Finding Campaign confirm that CD–35 2722 B is physically associated with the primary star. Near-IR spectra indicate a spectral type of L4 \pm 1 with a moderately low surface gravity, making it one of the coolest young companions found to date. The absorption lines and near-IR continuum shape of CD–35 2722 B agree especially well the dusty field L4.5 dwarf 2MASS J22244381–0158521, while the near-IR colors and absolute magnitudes match those of the 5-Myr old L4 planetary-mass companion, 1RXS J160929.1–210524 b. Overall, CD–35 2722 B appears to be an intermediate-age benchmark for L-dwarfs, with a less peaked *H*-band continuum than the youngest objects and near-IR absorption lines comparable to field

¹Institute for Astronomy, University of Hawaii, 2680 Woodlawn Drive, Honolulu, HI 96822

²Department of Astronomy, University of Oxford, DWB, Keble Road, Oxford OX1 3RH, U.K.

³Steward Observatory, University of Arizona, 933 North Cherry Avenue, Tucson, AZ 85721

⁴Gemini Observatory, Southern Operations Center, c/o AURA, Casilla 603, La Serena, Chile

⁵University of Rochester, Department of Physics & Astronomy, Rochester, NY 14627-0171, USA

⁶Jet Propulsion Laboratory, MS 169-506, 4800 Oak Grove Drive, Pasadena, CA 91109

⁷Space Telescope Science Institute, 3700 San Martin Drive, Baltimore, MD 21218

⁸Department of Terrestrial Magnetism, Carnegie Institution of Washington, 5241 Broad Branch Road, NW, Washington, DC 20015

⁹Departamento de Física - ICEx - Universidade Federal de Minas Gerais, Av. Antonio Carlos, 6627, 30270-901, Belo Horizonte, MG, Brazil

¹⁰University of Toronto at Scarborough, 1265 Military Trail, Toronto, Ontario M1C 1A4, Canada

¹¹Universidade de São Paulo, IAG/USP, Departamento de Astronomia, Rua do Matao, 1226, 05508-900, São Paulo, SP, Brazil

¹²Tokyo Institute of Technology, 2-12-1 Ookayama, Meguro-ku, Tokyo 152-8550

¹³NASA Goddard Space Flight Center, Exoplanets and Stellar Astrophysics Laboratory, Greenbelt, MD 20771

¹⁴Department of Astronomy and Astrophysics, University of California, Santa Cruz, CA, USA

¹⁵Mauna Kea Infrared, LLC, 21 Pookela St., Hilo, HI 96720

objects. We fit Ames-Dusty model atmospheres to the near-IR spectra and find $T_{eff} = 1700\text{--}1900$ K and $\log(g) = 4.5 \pm 0.5$. The spectra also show that the radial velocities of components A and B agree to within ± 10 km/s, further confirming their physical association. Using the age and bolometric luminosity of CD–35 2722 B, we derive a mass of $31 \pm 8 M_{Jup}$ from the Lyon/Dusty evolutionary models. Altogether, young late-M to mid-L type companions appear to be overluminous for their near-IR spectral type compared to field objects, in contrast to the underluminosity of young late-L and early-T dwarfs.

1. Introduction

Currently, more than 440 extrasolar planets have been discovered by radial velocity and transit techniques, orbiting at relatively small separations (< 5 AU) from their parent stars (e.g. Butler et al. 2006; Marcy et al. 2008; Mayor et al. 2009). In contrast, direct-imaging surveys are sensitive to Jupiter-mass planets at separations of $\gtrsim 10$ AU around nearby stars (~ 25 pc) when they are young ($\lesssim 100$ Myrs) (e.g. Biller et al. 2007; Lafrenière et al. 2007; Nielsen & Close 2010). So far, these searches have mostly yielded brown dwarf or planetary-mass objects at large separations (Chauvin et al. 2005a; Luhman et al. 2006; Lafrenière et al. 2008; Thalmann et al. 2009). Spectroscopic studies of the atmospheres of the brighter companions are revealing their temperatures, gravities and masses (Lavigne et al. 2009; Bonnefoy et al. 2010). However, even more exciting discoveries of planetary-mass objects at 5–120 AU separations are beginning to come forth (Marois et al. 2008; Kalas et al. 2008; Lagrange et al. 2010). Since these companions have separations that allow us to isolate their photons from those of the primary, we can begin to characterize the atmospheres of the companions discovered by direct imaging (Bowler et al. 2010).

Since December 2008, we have been conducting the Gemini NICI Planet-Finding Campaign to find and characterize planets through direct imaging (Liu et al. 2010). The Campaign is a three-year program at the Gemini-South 8.1-m Telescope to directly image and characterize gas-giant planets around 300 nearby stars. The NICI instrument was specifically designed for this purpose (Ftaclas et al. 2003; Chun et al. 2008). It is equipped with an 85-element curvature adaptive optics system, a Lyot coronagraph, and a dual-camera system capable of simultaneous spectral difference imaging (Racine et al. 1999, SDI) on and off the $1.6\ \mu\text{m}$ methane feature seen in cool (< 1400 K) substellar objects (e.g. Burrows et al. 1997; Baraffe et al. 2003). The two cameras are equipped with Aladdin II InSb detectors and have $18.43'' \times 18.43''$ field of view and a plate scale of 18 mas/pixel (milli-arcseconds/pixel). NICI can also be used in a fixed Cassegrain Rotator mode for Angular Differential Imaging (ADI;

Liu 2004; Marois et al. 2005), where the telescope image rotator is turned off, so that the sky rotates on the detector while the telescope and instrument PSF (point spread function) artifacts remain fixed (See § 2.1.1).

In an earlier paper we presented the discovery of PZ Tel B, one of few young substellar companions directly imaged at orbital separations similar to those of giant planets in our own solar system (Biller et al. 2010b). Here we present the discovery of CD–35 2722 B, one of the coolest young (~ 100 Myr) close-separation (< 100 AU) brown dwarf companions to a star directly-imaged to date. Torres et al. (2008) identify CD–35 2722 A as a member of the AB Doradus association, based on its common space motion and consistent galactic location with the other association members. They derive a kinematic distance estimate of ~ 24 pc (See § 3.1). The eponymous star of the AB Doradus association itself appears to be coeval with the Pleiades, which is thought to be younger than 150 Myrs (Barrado y Navascués et al. 2004; Burke et al. 2004; Ortega et al. 2007), and other studies conclude that AB Dor is approximately 50 Myr or older (Zuckerman et al. 2004; Close et al. 2007). Thus, we adopt an age of 100 ± 50 Myr for CD–35 2722 A based on its membership in the AB Dor group.

2. Observations and Data Reduction

2.1. Gemini South/NICI imaging

2.1.1. Campaign Observing Modes and Data Reduction

We use two observing sequences for each target in the NICI Campaign to optimize our sensitivity to both methane-bearing and non-methane bearing companions. Both sequences employ the ADI technique (Liu 2004; Marois et al. 2005). Exposure times per frame are kept around 1 minute so that the noise is background-limited, and the total time spent on detector readouts is small. Observing hour angles are chosen such that the rotation rate of the sky is less than 1 degree per minute to avoid excessive smearing during an individual exposure. The total sky rotation over the observing sequence is also required to be greater than 15 degrees, to limit flux loss by self-subtraction of companions at small separations (e.g. Biller et al. 2009).

To search for close-in methane-bearing planets, we combine the Angular and Spectral Difference Imaging methods into a single unified sequence (“ASDI”). In this observing mode, a 50-50 beam splitter in NICI divides the incoming light between the off ($\lambda = 1.578 \mu\text{m}$) and on-methane ($\lambda = 1.652 \mu\text{m}$) moderate-bandwidth ($\Delta\lambda/\lambda = 4\%$) filters which pass the light into the two imaging cameras, henceforth designated the “blue” and “red” channels

respectively. The two cameras are read out simultaneously for each exposure. The red channel image is subtracted from the blue channel image to remove the nearly identical quasi-static speckles in the two channels. The resulting difference image has drastically improved sensitivity to methane-bearing objects, which are expected to be much fainter in the red channel (methane-absorbed) than in the blue channel. In the ASDI mode, we take 45 1-minute frames.

At larger separations ($\gtrsim 1.5''$), our sensitivity is limited by throughput, not by speckle noise. Thus we also obtain an ADI sequence without the 50-50 beam splitter, sending all the light to the blue channel, in order to achieve maximum sensitivity. In this mode, we take 20 1-minute frames using the standard *H*-band filter, which is roughly four times wider than the 4% methane on/off filters.

The initial image processing steps in the NICI Campaign data reduction pipeline were applied to all raw images. After bad pixel removal and flat-fielding, distortion corrections were applied. To determine the distortion, we acquired images of a rectangular pinhole grid placed upstream of the NICI AO system. Deviations of the imaged pinhole (spot) centers from a rectangular grid were used to measure the optical distortion of the blue and red channels. First, we fit a model rectangular grid of points to the spot centroids, allowing for rotation, change in grid spacing (different in x and y directions) and translation. Next, we found the 2nd order transformation in the coordinates of the observed spot centers that match the coordinates of the fitted model grid. The RMS in the difference between the distortion-corrected spot centroids and the rectangular model grid centroids was 0.1 pixels. Distortion-corrected images were then constructed by replacing the values at the original coordinates with interpolated values at the transformed coordinates using cubic interpolation.

In NICI data, the translucent focal plane mask causes arc-like features to appear near the half transmission radius ($r = 0.32''$) of the Gaussian-profiled mask, which are dissimilar between the blue and red channels. Thus, for the ASDI and ADI datasets, we applied a filter to the images to remove arc-like PSF features centered on the primary star. For every pixel in the image, we computed the interpolated value at 100 points evenly spaced along an arc centered on the primary star and extending 30 pixels in azimuth around the chosen pixel. The median of these 100 values was then subtracted from the pixel value. This filtering process improves the quality of channel differencing during the ASDI and ADI reductions.

An additional filter was applied to remove the stellar halo. Each individual image was smoothed with a Gaussian of 8 pixel FWHM and subtracted from the original (unsharp masking). Next, all the (unsharp masked) images were smoothed with a Gaussian of 2 pixel FWHM. With this 2-step smoothing process, all spatial features that are significantly

different in size from the FWHM ~ 3 pixel NICI PSF were removed from the images.

2.1.2. *ADI and ASDI Observations*

CD–35 2722 was first observed on UT January 16, 2009 in the standard campaign observing modes (ASDI and ADI). The NICI images revealed a bright companion candidate with separation $\approx 3''$. For astrometric follow-up, we observed the system again on UT January 10, 2010 in the ASDI mode. Since the companion has separation $> 1''$ and does not have methane, we reduced the blue and red channel data sets separately using a simple ADI data reduction method and then added the reduced images together. For each channel, all the images were registered using the primary star, which was detected at very high signal to noise through the partially transmissive focal plane mask. The images were median combined to build a PSF image. This image consisted only of quasi-static speckles, since any real objects in the dataset would appear at different PAs in the individual images (since the rotator is off) and would be removed by the median process. Next, the PSF image was matched to and subtracted from each of the 45 individual frames, fitting for the optimal translation and intensity normalization to match the speckle patterns between $0.65''$ and $0.78''$ from the star. This fitting region lies well outside the mask edge at $0.51''$. The final reduced image was constructed by rotating the individual subtracted images to place North up, registering them using the previously computed positions of the primary star, and median combining the stack. The PAs recorded in the FITS header of each frame give the orientation at the beginning of the exposures, but we calculated and used the PAs at mid-exposure to align our images. Finally, the reduced blue and red channel images were added together. We show a cutout from the final reduced image for the 2010 data in Figure 1.

2.1.3. *JHK_S Rotator-On Photometric Observations*

Upon detection of the very bright candidate at a separation of $\approx 3''$, we obtained images in the JHK_S filters on UT March 9, 2009 to measure its near infrared colors. The broad band filters in NICI are in the MKO (Mauna Kea Observatory) system (Simons & Tokunaga 2002; Tokunaga & Vacca 2005). The observations were obtained in the rotator-on mode. Nine 15-second exposures were taken, imaging the star simultaneously in both channels, with the H filter in the blue channel and the K_S filter in the red channel. Nine 15-second exposures with the J filter in the blue channel were taken immediately following these observations. For the reduction of the JHK_S rotator-on data, we flat-fielded and registered the frames on the stellar centroid and median combined the stack of images. Cutouts from the reduced

images of CD–35 2722 in the J , H and K_S -bands are shown in Figure 2. To determine the JHK band flux ratios of the companion relative to the primary, we first used simple aperture photometry (3 pixel radius) to measure the relative fluxes of the companion and the primary star, with the latter seen under the focal plane mask.

To determine the transmission of NICI’s coronagraphic mask, we imaged a pair of field stars, $4.2''$ apart on UT October 31, 2010. The stars, 2MASS J06180157–1412573 ($H=9.46$ mag) and 2MASS J06180179–1412599 ($H=11.16$ mag) were chosen so that they could be imaged at the same time without saturating either. Ten images were obtained in the H and K -bands, with the brighter star under the mask, followed by 10 images with both stars off the mask. In the J -band, 4 images were taken in each configuration. All images were taken with the Cassegrain rotator on, and thus there was no smearing during individual exposures. We then computed the ratio of the aperture (3 pixel radius) fluxes of the two stars, in both the on and off-mask configurations. The off-mask flux ratio divided by the on-mask flux ratio yields the mask attenuation. We determined that the central attenuation of the $0.32''$ mask is 6.37 ± 0.06 , 5.94 ± 0.02 and 5.70 ± 0.03 magnitudes in the J , H and K_S -bands, respectively. The uncertainties are the RMS of the central attenuation measurements for the individual images in each filter.

These attenuation factors were applied to the raw flux ratio to arrive at the final JHK_S flux ratios. We computed the uncertainty in the flux ratios by including the dispersion in the flux ratios over the data set and the uncertainties in the focal plane mask transmission. To convert the K_S -band photometry of the companion to the K -band filter (a very small effect), we applied the transformations from Stephens & Leggett (2004). Table 1 lists the final NICI photometry of CD–35 2722 B.

2.2. IRTF/SpeX Imaging

We also obtained images of CD–35 2722 with the infrared guide camera of the facility spectrograph, SpeX, of the 3-m NASA Infrared Telescope Facility (IRTF) on UT February 3, 2010 and UT September 24, 2010 in good seeing conditions. We obtained images in the JHK bands, using 5 dither positions for each filter. The IRTF/SpeX images were flat-fielded, sky-subtracted, registered and stacked. To measure the flux ratio of the primary and the companion we first removed the background flux near the companion that comes from the primary. This was achieved by applying the same filter used in § 2.1.1 to remove arc-like features in the NICI PSF, except that medians were taken over arcs of length 90 pixels, instead of 30. Then flux ratios between the primary and the companion were computed using apertures of 6 pixel radii. To assess the error in our measurements and any flux loss from the

filtering process, a hundred simulated companion images were created by scaling down the primary to the flux level of the secondary and shifting them to the same separation, placed with uniform azimuthal spacing, but at $>20^\circ$ difference in PA (>10 pixels away) compared to the actual companion. Photometry was done on the known positions of the simulated companions after the filtering process was applied. The RMS in the measurements was taken as the photometric error. We also computed the estimated flux loss from the mean of the differences between the known and measured photometry of the 100 simulated companions. These loss fractions were ~ 0.03 magnitudes, and we corrected for this loss in each band. Even though the two epochs of IRTF measurements agree to better than 0.02 magnitudes, to be conservative we adopt the errors from the simulations, and list the mean of the photometry from the two epochs in Table 1.

The primary star could be variable and thus use of the non-contemporaneous 2MASS photometry to derive the magnitudes of CD–35 2722 B from our flux ratio measurements may not be appropriate. Thus we observed a standard star in *JHK* during our 2nd epoch IRTF observations on UT September 24, 2010. We measured *JHK* MKO magnitudes of 7.85 ± 0.03 , 7.31 ± 0.05 and 7.07 ± 0.01 mag for CD–35 2722 A, which agree with the 2MASS-derived measurements to within 1σ (see Table 1). Moreover, other available data do not strongly indicate variability. Optical monitoring of CD–35 2722 A shows variability with an amplitude of $\Delta V = 0.11$ – 0.12 mag and a period of 1.7 days (Pojmanski 2003; Messina et al. 2010). This is likely due to rotating spots on the surface of this young star, in which case the photometric amplitude should be smaller in the near-IR.

2.3. Gemini North/NIFS Spectra

Spectroscopic follow-up observations were obtained with NIFS (McGregor et al. 2003) on the Gemini-North telescope. The target was observed with the *J*, *H* and *K* settings of NIFS, which cover 1.15 – 1.33 μm , 1.49 – 1.80 μm and 1.99 – 2.40 μm , respectively, at spectral resolutions of $\Delta\lambda/\lambda = 5000$ – 6000 . Table 3 gives a log of the observations. The primary star was used as the AO natural guide star, providing significant correction of the atmospheric turbulence. Due to the southern declination of the target ($\text{DEC} \sim -36^\circ$), the observations were carried out at high airmasses of 1.8 – 2.0 . The average FWHM obtained was $0.15''$.

The data were taken in a 'ABBA' nodding sequence, with the object dithered by $1.5''$ between two positions in the field of view. The data were reduced with the Gemini NIFS IRAF pipeline, following the standard procedures to produce a wavelength and distortion-corrected data cube. The sky background was removed from A frames by subtracting the negative of the nearest B frame, and vice versa. Figure 3 shows CD–35 2722 B in an A–B

NIFS image.

Spectra of the object were then extracted from each cube with the `nfextract` routine, using an aperture of $0.5''$. The wavelength solution for the 1-d spectra was checked against night sky lines (by re-running the reduction procedure *without* the sky subtraction), and re-interpolated where necessary. We found small drifts in the wavelength solution between nights on the order of $\approx 2 \text{ \AA}$.

Telluric standard stars of spectral type A0V were observed at similar airmass to the science observations and were reduced in the same way. Stellar features (hydrogen lines) were removed with the IDL package `spextool` (Cushing et al. 2004). The resulting telluric spectrum was then used to correct each individual science spectrum before combining them.

The individual science spectra were scaled and combined using a 3-sigma clipped mean, with the rms per wavelength bin used to estimate the noise in the resulting combined spectrum. The combined spectrum was then multiplied by the filter curves for the Gemini *JHK* filters, while the total flux in each band was set to the *JHK* photometry measured by NICI. The calibrated *JHK* spectra are shown in Figure 4.

3. Results

3.1. Astrometric Confirmation of CD-35 2722 B

Two objects were detected in the CD-35 2722 field at separations of $3.172 \pm 0.005''$ and $5.312 \pm 0.011''$ from CD-35 2722 A on UT January 16, 2009 and again at separations of $3.137 \pm 0.005''$ and $5.316 \pm 0.011''$ on UT January 10, 2010. Since the coronagraphic mask is not completely opaque, we should be able to measure the position of both the primary star and the candidate to better than a tenth of a pixel, given the signal to noise of the detections and the accuracy of our centroiding algorithm. However, our astrometry is limited by the uncertainty in our measurement of the image distortion. Comparison of two epochs of dense star field images shows the astrometric discrepancy between epochs was ~ 0.3 pixel at $3''$ and ~ 0.6 pixel at $6''$ and we incorporate these errors in our astrometry in Table 2.

To check whether these astrometric measurements are consistent with the motions of background objects, we need the proper motion and the distance to the primary. The proper motions for CD-35 2722 A in RA and DEC are -5.6 ± 0.9 and -56.6 ± 0.9 mas/year, respectively (Zacharias et al. 2009).

Using the CAPScam/duPont telescope at Las Campanas Observatory (Boss et al. 2009), we obtained 3 epochs of parallax observations separated by 8 months (April 2010, November

2010, December 2010). This yielded a trigonometric parallax of 47 ± 3 mas (21.3 ± 1.4 pc). Three is the minimum number of observations required to measure a parallax. Thus it is difficult to properly assess the uncertainty in our measurement. So we estimated the error using a Monte Carlo approach, assuming a conservative 1.5 mas precision on each epoch and fitting the parallax and proper motion of 10,000 Monte Carlo realizations of the data. Further observations are in progress and a definitive value will be published in Anglada-Escudé et al. 2010 (in preparation).

The mean distance to the AB Doradus group nucleus has been refined in a new investigation of the moving groups within 100 pc of the Earth (see Mamajek 2010). The kinematic analysis therein employs the space motions of only the group members with Hipparcos parallaxes (van Leeuwen 2007) and the highest quality radial velocity measurements to find a distance of 20.6 ± 2.4 pc for 8 “nuclear” members. Comparing the AB Dor group space motions and the CD–35 2722 A proper motion, we see that the star is very likely also a “nuclear” AB Doradus member and thus at the same distance. We note that this distance estimate is in agreement with our parallax measurement. The predicted radial velocity from the best-fit space motions is 31.5 ± 1.4 km/s. This is completely consistent with the published measurement of 31.4 ± 0.4 km/s (Torres et al. 2006).

In Figure 5, we compare the motions of the two objects in the CD–35 2722 field to the expected motion of a background object given the first epoch astrometry, the known proper motion and estimated distance to CD–35 2722 A. The change in the PA of CD–35 2722 B is significantly different (at the 3σ level) from that expected of a background object. This indicates that CD–35 2722 B is physically associated with the primary, although about 1.6 AU/year of orbital motion is required to explain the relative motion with CD–35 2722 A. In comparison, the second object in the field at $\approx 5.3''$ separation moves as expected for a background object, thus confirming the joint accuracy of the proper motion and parallax of CD–35 2722 A and our NICI astrometric calibration. (See also Biller et al. 2010.)

Since the viewing angle and eccentricity of companion’s orbit are unknown, we estimate its semi-major axis by applying a statistical correction from Dupuy & Liu (2010). Assuming a uniform distribution of orbital eccentricities from 0 to 1, we multiply the projected physical separation by $1.1_{-0.36}^{+0.9}$ to estimate the true semi-major axis. Applying this factor to CD–35 2722 B’s measured separation, we obtain an estimated orbital semi-major axis of 83_{-33}^{+69} AU. We derived a mass of $0.4M_{\odot}$ for CD–35 2722 A using its age and absolute H mag with Siess et al. (2000) evolutionary models. Using this mass with Kepler’s Third Law we obtain a period of 1195_{-710}^{+1490} years for component B. The observed motion of the companion (1.6 AU over 1 year) is plausible for a bound object.

3.2. Near-IR Colors and Metallicity

To measure colors of CD–35 2722 A, we convert our relative flux ratio measurements (§ 2.1.3 and § 2.2) into apparent magnitudes for CD–35 2722 B using the 2MASS photometry. The *JHK*-band IRTF/SpeX data yielded more accurate flux ratios than the NICI observations, because the IRTF photometry did not incur the additional uncertainty of the NICI focal plane mask transmission; thus, we use the IRTF-derived results for the photometry of CD–35 2722 B. However, the NICI images provide far better astrometry than the IRTF data. Table 1 summarizes the resulting magnitudes for CD–35 2722 B.

Figure 6 compares the near-IR colors of CD–35 2722 B with other stellar and substellar objects, including old (high-gravity) field ultracool dwarfs and young (lower-gravity) objects found in the field and as companions. The *JHK* colors of CD–35 2722 B agree well with known late-M and L dwarfs.

A metallicity measurement for the primary star is relevant to constraining the formation of CD–35 2722 B. However, we see that CD–35 2722 A has $[\text{Fe}/\text{H}] = 0.04 \pm 0.05$ dex (Viana Almeida et al. 2009), which is close to the mean $[\text{Fe}/\text{H}]$ of the solar neighborhood, -0.05 dex (Johnson & Apps 2009). As a consistency check, we make an indirect estimate of the metallicity of CD–35 2722 A using the photometric calibration of Johnson & Apps (2009). Following their method, we determined the $[\text{Fe}/\text{H}]$ of CD–35 2722 A from its height above the main-sequence isochrone in a plot of M_K versus $V - K$. Since M1 dwarfs reach the main sequence by 100 Myr (Siess et al. 2000), the comparison of CD–35 2722 A with nearby main-sequence stars is appropriate. We derived an $[\text{Fe}/\text{H}]$ of 0.0 ± 0.16 dex for CD–35 2722 A, consistent with the published value. An alternate calibration of the metallicity is found in Schlaufman & Laughlin (2010), who use a volume-limited and kinematically matched sample of F and G dwarfs from the Geneva-Copenhagen Survey to infer the mean metallicity of M dwarfs in the Solar Neighborhood and base their final calibration purely on high-resolution spectroscopy of FGK primaries with M dwarf companions. Using their method, we derived an $[\text{Fe}/\text{H}]$ of -0.12 ± 0.16 dex for CD–35 2722 A, again consistent with a solar metallicity.

3.3. Spectral Analysis

3.3.1. Spectral Typing

To derive an empirical spectral type for CD–35 2722 B, we compared our Gemini/NIFS spectra to field L dwarfs from the IRTF Spectral Library (Cushing et al. 2005; Rayner et al.

2009) and young L dwarfs from recent studies (Figure 7). When comparing to lower resolution spectra (IRTF prism $R=150$, IRTF SpeX $R=2000$), we convolved our NIFS spectrum with a Gaussian of appropriate width. Since the field dwarfs are old objects, we expect some mismatch with CD–35 2722 B in surface gravity dependant spectral features.

The best matched spectra we find is from the L4.5 dwarf 2MASS J22244381–0158521, which is believed to have an unusually dusty atmosphere (see Stephens et al. 2009). We note that almost every absorption line feature is well-matched between this dusty field object and CD–35 2722 B. However the NIR colors of CD–35 2722 B are a little bluer than those of 2MASS J22244381–0158521 ($H - K=0.77$ vs 0.86 and $J - H=0.86$ vs 1.05; see Figure 6). The young (≈ 5 Myr) L4 planet 1RXS J160929.1–210524 b(Lafrenière et al. 2008, 2010) exhibits a narrower H -band shape than the CD–35 2722 B spectra, but the JHK absolute magnitudes and $J - H$ and $H - K$ colors of the two objects agree completely within errors.

The field L3 and L5 dwarfs show clear differences in line strengths, continuum shape and flux level in the K -band. The CD–35 2722 B spectrum also shows signs of youth in that the shape of its H -band spectra is more triangular than that of field L dwarfs, as seen in young L-type dwarfs (Lucas et al. 2006; Kirkpatrick et al. 2006; Allers et al. 2007) However, the H -band shape is also less peaked than the young L dwarfs 1RXS J160929.1–210524 b (~ 5 Myr; Lafrenière et al. 2010) and G196-3 B (≈ 100 Myr; Rebolo et al. 1998, Shkolnik et al. 2009). Overall, CD–35 2722 B does not seem to have especially low surface gravity, since the strength of its FeH lines and K I lines are comparable to those of field dwarfs.

Since the L3 and L5 spectra already differ significantly from that of CD–35 2722 B, we assign CD–35 2722 B a spectral type of $L4\pm 1$. We also derive consistent spectral types of L2.5, L3.5, L3.5 and L4 using spectral indices from the literature: H_2O $1.53\mu m$ (1.27 ± 0.05 ; Allers et al. 2007), H_2OA (0.56 ± 0.03 ; McLean et al. 2003), H_2OC (0.65 ± 0.03 ; McLean et al. 2003), and CH_4 $2.2\mu m$ (0.946 ± 0.005 ; Geballe et al. 2002), respectively.

We also tried to find the best matched spectra to CD–35 2722 B from the > 400 M, L, and T dwarfs in the online archive of SpeX Prism data (e.g. Burgasser & McElwain 2006), by scaling relative flux levels to minimize χ^2_ν . To match the low-resolution SpeX spectra, our NIFS spectra are first Gaussian smoothed. At this lower resolution, most features of the spectra are no longer visible, and so fits rely mainly on the shape of the continuum. Nevertheless, we observe a clear minimum in the χ^2_ν value for spectral types between L3 and L6. We verified the fits by eye to check that the χ^2_ν minima were sensible. The closest matches to our smoothed spectra, in order of increasing χ^2_ν are 2MASS J20025073–0521524 (L6, Burgasser et al. 2008), SDSS J232804.58-103845.7 (L3.5, Chiu et al. 2006), 2MASSW J0205034+125142 (L5, Reid et al. 2006) and 2MASS J21512543 -2441000 (L3,

Burgasser et al. 2008).

With a spectral type estimate for CD–35 2722 B in hand, we compare its NIR luminosities with those of field MLT dwarfs, and other young MLT dwarfs with measured parallaxes (see Figure 9). CD–35 2722 B is over-luminous by ~ 1 mag compared to L4 field dwarfs in the JHK-bands. As noted earlier, its NIR luminosities are indistinguishable from those of the 5 Myr old planet, 1RXS J160929.1–210524 b. The young L4 dwarfs 130948 B and C (age ~ 790 Myr, Dupuy et al. 2009a) are also over-luminous by ~ 0.5 mags. Young late-L and early-T companions are clearly under-luminous compared to old objects, as previously noted by Metchev & Hillenbrand (2006) and Bowler et al. (2010), while the young late-M to mid-L companions are overluminous. The young L1 dwarf, AB Pic b (age ~ 30 Myr, Torres et al. 2008) seems under-luminous and thus unlike other young M7–L5 dwarfs.

3.3.2. Model Atmosphere Fitting

To constrain the atmospheric properties of CD–35 2722 B, we compare our NIFS spectrum to the Ames-Dusty synthetic spectra of Allard et al. (2001). For each model spectrum in the Dusty grid, the flux of the model is adjusted to minimize the χ^2_ν value of the fit to the observed spectrum. The overall minimum χ^2_ν value across all template spectra in the grid gives the best-fit model (Figure 8). We find the smallest χ^2_ν values for $T_{\text{eff}} = 1700\text{--}1900$ K with $\log(g) = 4.5\text{--}6.0$. Since, Ames-Dusty models are not able to reproduce very well the spectra of cooler objects near the L-T transition, the lower temperature bound should not be taken as a very strong constraint. Nevertheless, using models from Saumon & Marley (2008), Cushing et al. (2008) are able to fit the spectra of L4 and L5 dwarfs with their $T_{\text{eff}}=1700$ K, $\log(g)=4.5$ models and L6 dwarfs with their $T_{\text{eff}}=1400$ K, $\log(g)=4.5$ atmospheric models, achieving good-fits past spectral type L8. This suggests that our lower bound of $T_{\text{eff}}=1700$ K is reasonable. Our temperature estimate is also consistent with the temperature we derive from the Lyon/Dusty evolutionary models in § 3.4.

Since χ^2_ν values depend more on the quality of matches between the shapes of the continuum rather than matches between specific spectral features, we also judge the best-fit models by eye. Examining the fits, we note that while no single model is a perfect match to the CD–35 2722 B spectra, the 1700K, $\log(g) = 4.5$ model reproduces the overall continuum shape from J to K rather well (Figure 8). At the same time, the shape and the depth of the two sets of K I doublets at 1.17 and 1.25 μm and the FeH lines in the J -band are clearly better reproduced in the 1700 K model than in other models. Moreover, given the young age of the system, we expect it to have a low surface gravity. The lower gravity of the 1700 K, $\log(g) = 4.5$ model is also consistent with the value estimated from the Lyon/Dusty

evolutionary model using our bolometric luminosity and age estimates (§ 3.4). Since the quality of the J -band fits are clearly much worse for the 1700 K, $\log(g)=4.0$ and $\log(g)=5.0$ models, we estimate a $\log(g)=4.5\pm0.5$ for CD–35 2722 B.

We also computed χ^2_ν from the fits to L dwarf models with clouds presented in Burrows et al. (2006). The shapes of the continua and the relative fluxes in the JHK -bands are completely consistent between these models and the CD–35 2722 B spectra. The strengths of the K I doublets in the J -band are also consistent. The χ^2_ν results show a clear minima in the T_{eff} – $\log(g)$ space, and we estimate $T_{\text{eff}}=1700\pm100$ K, and $\log(g)=4.5\text{--}5.0$ from the Burrows models. The H -band peaks in the models are, however, clearly rounder with more flux at the blue end compared to the CD–35 2722 B spectra due to the absence of FeH features in the models. The models also show stronger water absorption at the red end of the H -band. Moreover, the models are deficient in Fe and FeH features in the J -Band, and their CO features in the K -band are too strong. The cloud-free models from Burrows et al. (2006) have very different continua shape from the CD–35 2722 B spectra, and a reasonable match was not found.

3.3.3. Radial Velocities

Due to the dither pattern in the first set of J -band observations, there was enough light in the NIFS data to extract a spectrum of CD–35 2722 A. We used this spectrum to test whether CD–35 2722 A and B share the same radial velocity. The spectral types of the two objects are sufficiently different that cross-correlation techniques are not easily applied. Instead, we fit Gaussians to four strong K I lines in the J band, taking the average of the centroids as our measure of radial velocity. We find that the velocities of A and B agree to within the errors (±10 km/s) further confirming their physical association. The system velocity (25 ± 10 km/s) also agrees with the published value (31.4 ± 0.4 km/s, Torres et al. 2006) and the predicted value in § 3.1 within our errors.

3.4. Mass Estimates

We first determined the mass of CD–35 2722 B using the Lyon/Dusty evolutionary models (Chabrier et al. 2000), based on the observed absolute magnitudes and estimated age. To compute the mass and its associated uncertainty, we used a Monte Carlo technique, drawing the input values for M_J and age from random distributions. Values for M_J were chosen from a normal distribution corresponding to the photometry in Table 1. Age values were

chosen from a uniform distribution between 50 and 150 Myrs, as estimated for the AB Doradus association (Zuckerman et al. 2004; Luhman et al. 2005; Close et al. 2007). Using the Lyon/Dusty evolutionary models in the MKO photometric system (I. Baraffe, private communication), we computed the mass of CD–35 2722 B from 10,000 random trials, resulting in an adopted mass of $31 \pm 7 M_{Jup}$ from the median and standard deviation of the trials. Using the same approach with our M_H and M_K measurements, we estimate masses of 30 ± 7 and $34 \pm 9 M_{Jup}$, respectively. Thus, CD–35 2722 B is probably a brown dwarf, if we follow the notional dividing line between planets and brown dwarfs set by the deuterium-burning limit of $13.6 M_{Jup}$ for solar metallicity.

To assess the uncertainty contributed by each input parameter (age, distance, and J mag) in our mass calculation, we also computed the mass of CD–35 2722 B by assuming two of the inputs were error-free. The mass uncertainty arising from the assumed age dominates over that from the distance, which in turn dominates over that from the J -band photometry (Table 4). Of course, this does not account for the systematic errors in the evolutionary models themselves, which are just now being rigorously tested (e.g. Stassun et al. 2007; Dupuy et al. 2009b).

A somewhat more robust way to derive the mass of CD–35 2722 B is to use its bolometric luminosity and age as inputs to the Lyon/Dusty evolutionary models, since bolometric luminosities are less susceptible to uncertainties in the model atmospheres than single band-pass fluxes (Chabrier et al. 2000). Using the J -band bolometric corrections from Liu et al. (2010) for spectral types of L3–L5 (§ 3.3) and the input distribution of M_J described above, we calculated the corresponding distribution of bolometric luminosities for CD–35 2722 B. Then, using the luminosity and age distributions with the evolutionary models, we obtained a mass of $31 \pm 8 M_{Jup}$, again using the median and standard deviation of the trials (Figure 10). The L_{bol} -derived masses from the H and K -bands were also $31 \pm 8 M_{Jup}$, which is expected since most of the mass uncertainty arises from the uncertainty in age. We adopt this L_{bol} -derived mass as our best estimate in Table 1, though the mass estimates from individual filters and from L_{bol} are completely consistent. Note that the same set of input data and evolutionary models give an effective temperature of 1980 ± 100 K and a surface gravity with $\log(g) = 4.54 \pm 0.13$ dex, in reasonable agreement with the results from model atmosphere fits to the near-IR spectra (§ 3.3).

Using the same methods as for the Lyon/Dusty models, we compare the age and luminosity of CD–35 2722 B to the models of Burrows et al. (1997, 2001) to estimate the mass, T_{eff} , and $\log(g)$ to be $36 \pm 6 M_{Jup}$, 2150 ± 90 K and 4.83 ± 0.13 dex, respectively.

An alternative means using evolutionary models to estimate the mass comes from using the age and effective temperature, with the latter estimated from model atmosphere fitting

of the NIR spectra (§ 3.3). We adopt a similar Monte Carlo approach, assuming a uniform distribution in T_{eff} from 1700–1900 K, and derive a mass of $23 \pm 5 M_{Jup}$. This is somewhat lower than the mass derived from $\{L_{bol}, \text{age}\}$. This discrepancy occurs because the model atmosphere-derived T_{eff} is ≈ 180 K cooler than the evolutionary model-derived T_{eff} above, leading to a lower mass.²

A third means to estimate the mass from the evolutionary models comes from the H-R diagram, namely using the bolometric luminosity and the estimated temperature. This is the least useful method, as small uncertainties in T_{eff} translate into large mass uncertainties, given the tightness of the model tracks on the H-R diagram. Assuming a normal distribution in luminosity and a uniform distribution in T_{eff} , we derive $11 \pm 7 M_{Jup}$. Figure 10 illustrates the observed properties of CD–35 2722 B relative to the model predictions for different pairs of observable properties.

The color-magnitude diagrams in Figure 11 compare the 50 and 150 Myr isochrones from the Lyon/Dusty and Lyon/COND (Baraffe et al. 2003) evolutionary models with the color and absolute magnitudes of CD–35 2722 B. In both plots, the M_J vs $J - H$ and the M_K vs $J - K$ diagram, the companion’s position is within 1σ of that of 22, 31 and $39 M_{Jup}$ Dusty model-simulated brown dwarfs at ages 50, 100 and 150 Myrs, respectively.

4. Conclusions

As part of the Gemini NICI Planet-Finding Campaign, we have discovered a substellar companion to the young M1V star CD–35 2722 A, a member of the AB Doradus association. High quality astrometry over one year confirms CD–35 2722 B as a bound companion, with a projected separation of $3.17''$ (67 ± 4 AU) in January 2009. We estimate a companion mass of $31 \pm 8 M_{Jup}$ by using its bolometric magnitude and age and the Lyon/Dusty evolutionary models. JHK photometry show that the system has L dwarf-like colors.

The 1.1–2.4 μm spectra of CD–35 2722 B reveal a low temperature and low surface gravity, as expected for the young age and low mass of the companion. The H -band continuum shows the triangular shape characteristic of young ultracool dwarfs, though intermediate in shape between the youngest known objects and old (field) objects. Through direct comparison with known objects, we derive a spectral type of L4±1, making CD–35 2722 B one

²A somewhat similar effect has been identified in the young (≈ 790 Myr) L4+L4 dwarf binary HD 130948BC, where the T_{eff} derived from evolutionary models using the age and luminosity are ≈ 150 –300 K hotter than expected from atmospheric model fitting for objects of similar spectral type. (A direct model fit to the HD 130948BC spectrum is not available.) See § 5.8 of Dupuy et al. 2009a.

of the coolest young substellar companions identified to date. We fit the spectra using the Ames-Dusty model atmospheres and derive $T_{eff} = 1700\text{--}1900$ K and $\log(g) = 4.5 \pm 0.5$ dex. These estimates are consistent with the Lyon/Dusty evolutionary model-derived temperature of 1980 ± 100 K and $\log(g) = 4.54 \pm 0.14$ dex. As a member of a moving group with a good age estimate, CD–35 2722 B serves as a valuable benchmark for calibrating age-dependent spectral effects in L dwarfs. Comparison with other young substellar companions shows that when using near-IR spectral types, the late-M to mid-L companions appear to be over-luminous compared to the field objects, while the late-L and early-T companions appear to be under-luminous.

The mass and separation of CD–35 2722 B are comparable to other known young star+substellar companion systems. TWA 5b ($20 M_{Jup}$, 98 AU; Lowrance 1999), GQ Lup B ($17 M_{Jup}$, 100 AU; Neuhauser et al. 2005) and Gl 229 B ($35 M_{Jup}$, 45 AU; Nakajima et al. 1995) all have masses and separations within 50% of that of CD–35 2722 B, and all have primaries of spectral type K7 or later. This similarity may be a hint that they share a common formation mechanism. In-situ formation by core accretion is not viable for such massive companions at such large separations, especially around an M star. Alternate theories do not provide easy pathways to the formation of substellar companions like CD–35 2722 B; for instance, formation by fragmentation of a prestellar core (Bate 2003) is difficult for the mass ratio and separation of CD–35 2722 AB. Formation via gravitational instability (Boss 1997, Rafikov 2005, Boss 2006, Stamatellos & Whitworth 2008) require large massive disks ($>0.2\text{--}0.35 M_{\odot}$) and thus also do not provide an obvious solution, given the low mass of the primary star. However, Jeans mass fragmentation of the interstellar molecular cloud may be able to explain stellar-substellar systems, e.g., as discussed by Zuckerman and Song (2009). Moreover, Boss (2001) found that dense molecular cloud cores with magnetic fields can collapse and fragment into multiple protostar systems with initial masses as low a Jupiter mass, i.e., even smaller than the companion to CD–35 2722 A. This suggests that the CD–35 2722 system might well have formed by the classic binary star formation mechanism of fragmentation of a collapsing dense molecular cloud core.

This work was supported in part by NSF grants AST-0713881 and AST-0709484. Our research has employed the 2MASS data products; NASA’s Astrophysical Data System; the SIMBAD database operated at CDS, Strasbourg, France; the M, L, and T dwarf compendium housed at DwarfArchives.org and maintained by Chris Gelino, Davy Kirkpatrick, and Adam Burgasser; and the SpeX Prism Spectral Libraries maintained by Adam Burgasser at <http://www.browndwarfs.org/spepxism>. We would also like to thank Guillem Anglada and Alycia Weinberger for their parallax measurements of CD–35 2722 A.

Facilities: Gemini-South (NICI), IRTF (SpeX).

REFERENCES

Allard, F., Hauschildt, P. H., Alexander, D. R., Tamanai, A., & Schweitzer, A. 2001, *ApJ*, 556, 357

Allers, K. N., Liu, M. C., Dupuy, T. J., & Cushing, M. C. 2010, *ApJ*, 715, 561

Allers, K. N., et al. 2007, *ApJ*, 657, 511

Baraffe, I., Chabrier, G., Allard, F., & Hauschildt, P. 2003, in IAU Symposium, Vol. 211, Brown Dwarfs, ed. E. Martín, 41

Barrado y Navascués, D., Stauffer, J. R., & Jayawardhana, R. 2004, *ApJ*, 614, 386

Biller, B., et al. 2009, in American Institute of Physics Conference Series, Vol. 1094, American Institute of Physics Conference Series, ed. E. Stempels, 425–428

Biller, B. A., Liu, M. C., Wahhaj, Z., & the NICI Campaign Team. 2010a, *ApJ*

Biller, B. A., et al. 2007, *ApJS*, 173, 143

—. 2010b, *ApJ*, 720, L82

Bonnefoy, M., Chauvin, G., Rojo, P., Allard, F., Lagrange, A., Homeier, D., Dumas, C., & Beuzit, J. 2010, ArXiv e-prints

Boss, A. P. 2001, *ApJ*, 551, L167

Boss, A. P., et al. 2009, *PASP*, 121, 1218

Bowler, B. P., Liu, M. C., Dupuy, T. J., & Cushing, M. C. 2010, *ApJ*, 723, 850

Burgasser, A. J., Liu, M. C., Ireland, M. J., Cruz, K. L., & Dupuy, T. J. 2008, *ApJ*, 681, 579

Burgasser, A. J., & McElwain, M. W. 2006, *AJ*, 131, 1007

Burke, C. J., Pinsonneault, M. H., & Sills, A. 2004, *ApJ*, 604, 272

Burrows, A., Hubbard, W. B., Lunine, J. I., & Liebert, J. 2001, *Reviews of Modern Physics*, 73, 719

Burrows, A., Sudarsky, D., & Hubeny, I. 2006, *ApJ*, 640, 1063

Burrows, A., et al. 1997, *ApJ*, 491, 856

Butler, R. P., et al. 2006, *ApJ*, 646, 505

Casagrande, L., Flynn, C., & Bessell, M. 2008, *MNRAS*, 389, 585

Chabrier, G., Baraffe, I., Allard, F., & Hauschildt, P. 2000, *ApJ*, 542, L119

Chauvin, G., et al. 2005a, *A&A*, 438, L29

—. 2005b, *A&A*, 430, 1027

Chiu, K., Fan, X., Leggett, S. K., Golimowski, D. A., Zheng, W., Geballe, T. R., Schneider, D. P., & Brinkmann, J. 2006, *AJ*, 131, 2722

Chun, M., et al. 2008, in Society of Photo-Optical Instrumentation Engineers (SPIE) Conference Series, Vol. 7015, Society of Photo-Optical Instrumentation Engineers (SPIE) Conference Series

Close, L. M., Thatte, N., Nielsen, E. L., Abuter, R., Clarke, F., & Tecza, M. 2007, *ApJ*, 665, 736

Cushing, M. C., Rayner, J. T., & Vacca, W. D. 2005, *ApJ*, 623, 1115

Cushing, M. C., Vacca, W. D., & Rayner, J. T. 2004, *PASP*, 116, 362

Cushing, M. C., et al. 2008, *ApJ*, 678, 1372

Dupuy, T. J., & Liu, M. C. 2010, *ApJ*

Dupuy, T. J., Liu, M. C., & Ireland, M. J. 2009a, *ApJ*, 692, 729

—. 2009b, ArXiv e-prints

Ftaclas, C., Martín, E. L., & Toomey, D. 2003, in IAU Symposium, Vol. 211, Brown Dwarfs, ed. E. Martín, 521

Gautier, III, T. N., et al. 2007, *ApJ*, 667, 527

Geballe, T. R., et al. 2002, *ApJ*, 564, 466

Golimowski, D. A., et al. 2004, *AJ*, 127, 3516

Johnson, J. A., & Apps, K. 2009, *ApJ*, 699, 933

Kalas, P., et al. 2008, *Science*, 322, 1345

Kirkpatrick, J. D., Barman, T. S., Burgasser, A. J., McGovern, M. R., McLean, I. S., Tinney, C. G., & Lowrance, P. J. 2006, *ApJ*, 639, 1120

Knapp, G. R., et al. 2004, *AJ*, 127, 3553

Lafrenière, D., Jayawardhana, R., & van Kerkwijk, M. H. 2008, *ApJ*, 689, L153

—. 2010, *ApJ*, 719, 497

Lafrenière, D., et al. 2007, *ApJ*, 670, 1367

Lagrange, A., et al. 2010, ArXiv e-prints

Lavigne, J., Doyon, R., Lafrenière, D., Marois, C., & Barman, T. 2009, *ApJ*, 704, 1098

Leggett, S. K., et al. 2006, *MNRAS*, 373, 781

—. 2010, *ApJ*, 710, 1627

Liu, M. C. 2004, *Science*, 305, 1442

Lodieu, N., Hambly, N. C., Jameson, R. F., & Hodgkin, S. T. 2008, *MNRAS*, 383, 1385

Lowrance, P. J., et al. 1999, *ApJ*, 512, L69

Lucas, P. W., Weights, D. J., Roche, P. F., & Riddick, F. C. 2006, *MNRAS*, 373, L60

Luhman, K. L., Stauffer, J. R., & Mamajek, E. E. 2005, *ApJ*, 628, L69

Luhman, K. L., et al. 2006, *ApJ*, 649, 894

—. 2007, *ApJ*, 654, 570

Mamajek, E. E. 2010, in *Bulletin of the American Astronomical Society*, Vol. 42, *Bulletin of the American Astronomical Society*, 473–+

Marcy, G. W., et al. 2008, *Physica Scripta Volume T*, 130, 014001

Marois, C., Doyon, R., Racine, R., Nadeau, D., Lafreniere, D., Vallee, P., Riopel, M., & Macintosh, B. 2005, *JRASC*, 99, 130

Marois, C., Macintosh, B., Barman, T., Zuckerman, B., Song, I., Patience, J., Lafrenière, D., & Doyon, R. 2008, *Science*, 322, 1348

Mayor, M., et al. 2009, *A&A*, 493, 639

McGregor, P. J., et al. 2003, in Society of Photo-Optical Instrumentation Engineers (SPIE) Conference Series, Vol. 4841, Society of Photo-Optical Instrumentation Engineers (SPIE) Conference Series, ed. M. Iye & A. F. M. Moorwood, 1581–1591

McLean, I. S., McGovern, M. R., Burgasser, A. J., Kirkpatrick, J. D., Prato, L., & Kim, S. S. 2003, *ApJ*, 596, 561

Messina, S., Desidera, S., Turatto, M., Lanzafame, A. C., & Guinan, E. F. 2010, ArXiv e-prints

Metchev, S. A., & Hillenbrand, L. A. 2006, *ApJ*, 651, 1166

Mohanty, S., Jayawardhana, R., Huélamo, N., & Mamajek, E. 2007, *ApJ*, 657, 1064

Nielsen, E. L., & Close, L. M. 2010, *ApJ*, 717, 878

Ortega, V. G., Jilinski, E., de La Reza, R., & Bazzanella, B. 2007, *MNRAS*, 377, 441

Pojmanski, G. 2003, *Acta Astronomica*, 53, 341

Racine, R., Walker, G. A. H., Nadeau, D., Doyon, R., & Marois, C. 1999, *PASP*, 111, 587

Rayner, J. T., Cushing, M. C., & Vacca, W. D. 2009, *ApJS*, 185, 289

Rebolo, R., Zapatero Osorio, M. R., Madruga, S., Bejar, V. J. S., Arribas, S., & Licandro, J. 1998, *Science*, 282, 1309

Saumon, D., & Marley, M. S. 2008, *ApJ*, 689, 1327

Schlaufman, K. C., & Laughlin, G. 2010, *A&A*, 519, A105+

Shkolnik, E., Liu, M. C., & Reid, I. N. 2009, *ApJ*, 699, 649

Siess, L., Dufour, E., & Forestini, M. 2000, *A&A*, 358, 593

Simons, D. A., & Tokunaga, A. 2002, *PASP*, 114, 169

Stassun, K. G., Mathieu, R. D., & Valenti, J. A. 2007, *ApJ*, 664, 1154

Stephens, D. C., & Leggett, S. K. 2004, *PASP*, 116, 9

Stephens, D. C., et al. 2009, *ApJ*, 702, 154

Thalmann, C., et al. 2009, *ApJ*, 707, L123

Tokunaga, A. T., & Vacca, W. D. 2005, *PASP*, 117, 421

Torres, C. A. O., Quast, G. R., da Silva, L., de La Reza, R., Melo, C. H. F., & Sterzik, M. 2006, A&A, 460, 695

Torres, C. A. O., Quast, G. R., Melo, C. H. F., & Sterzik, M. F. 2008, Young Nearby Loose Associations, ed. Reipurth, B., 757

van Leeuwen, F. 2007, A&A, 474, 653

Viana Almeida, P., Santos, N. C., Melo, C., Ammler-von Eiff, M., Torres, C. A. O., Quast, G. R., Gameiro, J. F., & Sterzik, M. 2009, A&A, 501, 965

Zacharias, N., et al. 2009, VizieR Online Data Catalog, 1315, 0

Zuckerman, B., Song, I., & Bessell, M. S. 2004, ApJ, 613, L65

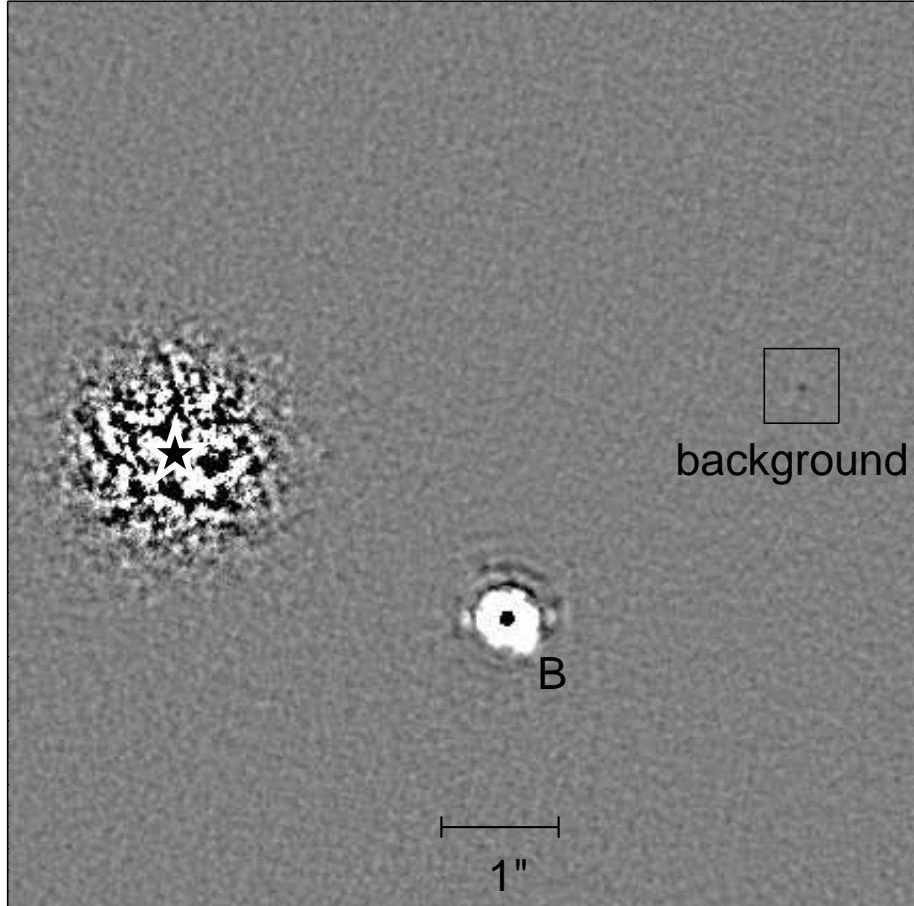


Fig. 1.— A cutout from the reduced NICI image of CD-35 2722, representing a 45-minute ADI observing sequence (North is up, East is left). This image is the sum of the reduced images from the blue and red channels (CH_4 4% short and long filters). The stellar position is indicated by a 'star' symbol. CD-35 2722 B was detected $3.137''$ away from the primary at a PA of 243.10° on UT Jan 10, 2010. The background object, shown in the square, had $5.316''$ separation and PA= 276.32° . The pixel intensities are shown in linear stretch from -4σ to 4σ , where σ is the pixel-to-pixel noise in background.

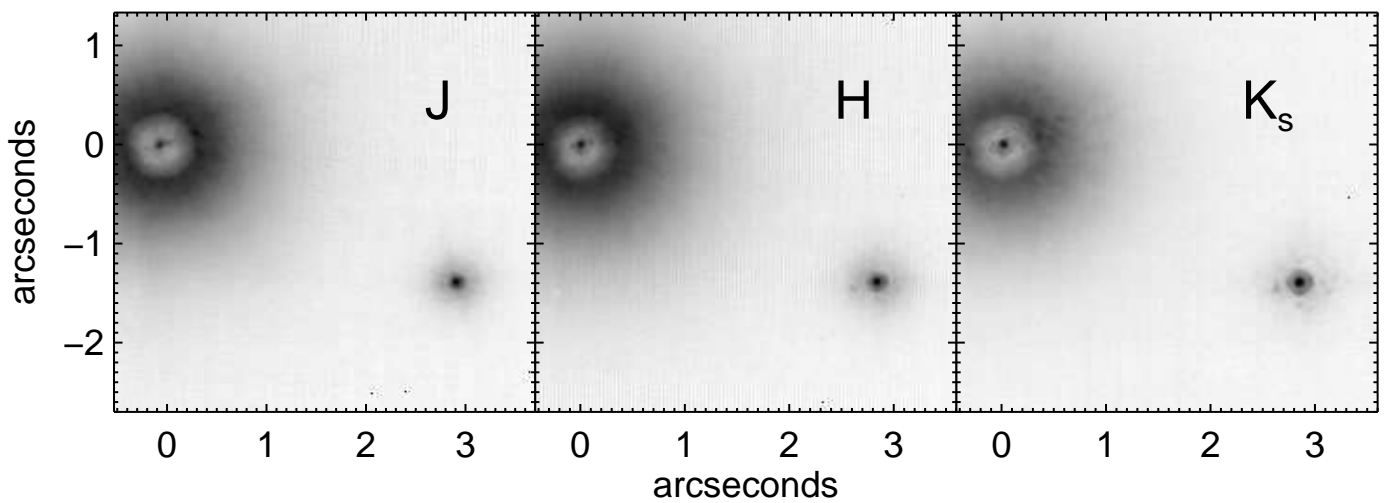


Fig. 2.— NICI images of CD-35 2722, obtained on UT March 9, 2009 in the J , H and K_s -band filters. North is up, East is left. The primary star, attenuated by the partially transmissive coronagraphic mask, is in the upper left area of the panels. CD-35 2722 B is in the lower right area, roughly $3''$ away from the primary.

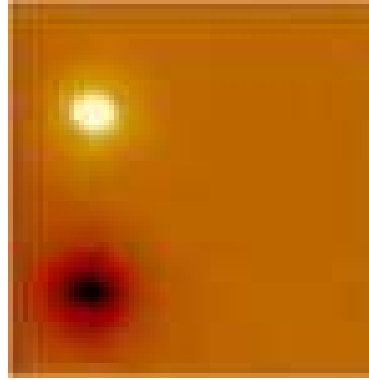


Fig. 3.— A NIFS A–B image of CD–35 2722 B with a $3.2'' \times 3.2''$ FOV. North is up, East is left. The primary, not shown in the image, lies above and to the left of this region.

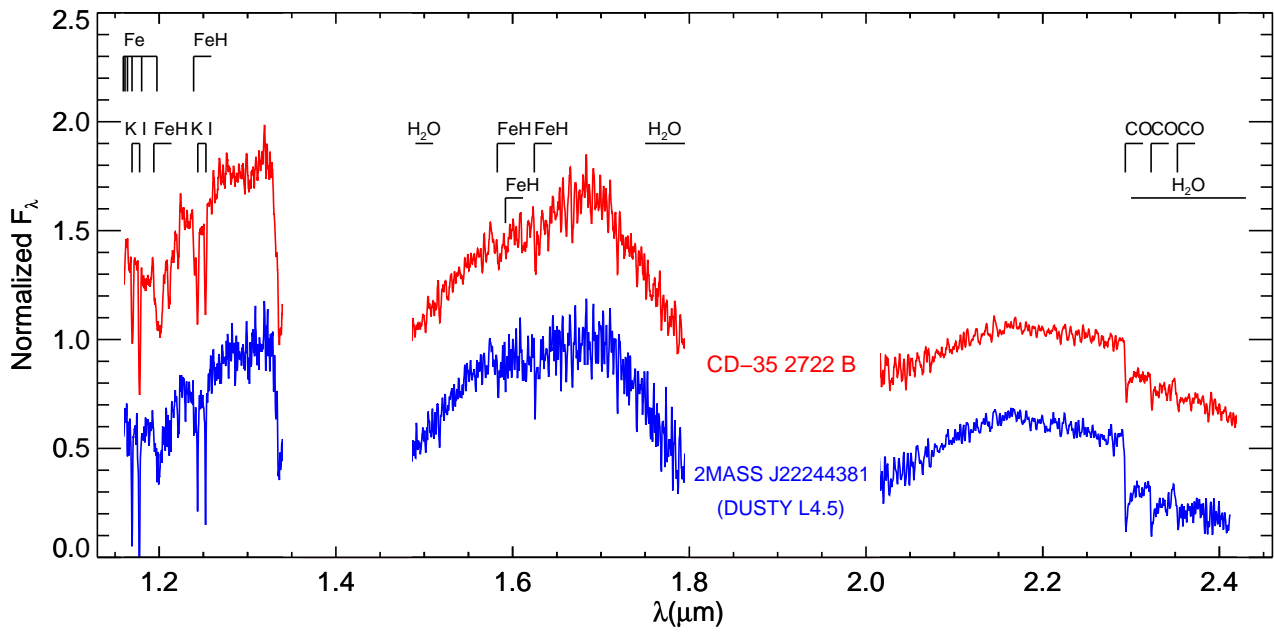


Fig. 4.— Normalized *JHK*-band NIFS spectra of CD–35 2722 B (red), plotted along with the dusty L4.5 dwarf 2MASS J22244381–0158521 (blue) (Knapp et al. 2004). Molecular features and line identifications are from Cushing et al. (2005).

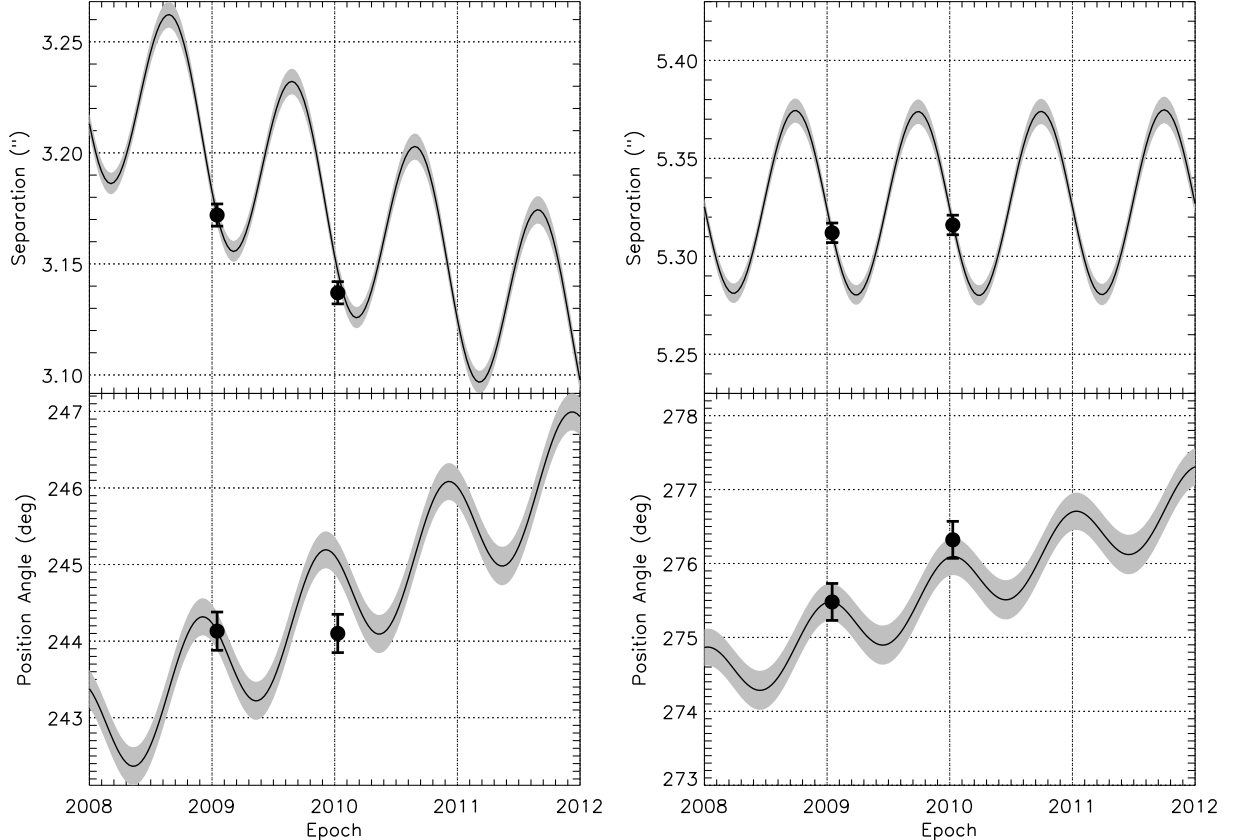


Fig. 5.— Comparisons of the observed motions of the two candidates (Left: CD-35 2722 B; Right: background object) to the expected motion of a background object given the first epoch astrometry, the proper motion and the distance of CD-35 2722 A. The very small observed change of the PA of CD-35 2722 B (bottom left panel) differs significantly (3σ) from that expected for a background object. The change in the position of the other candidate is consistent with a background object.

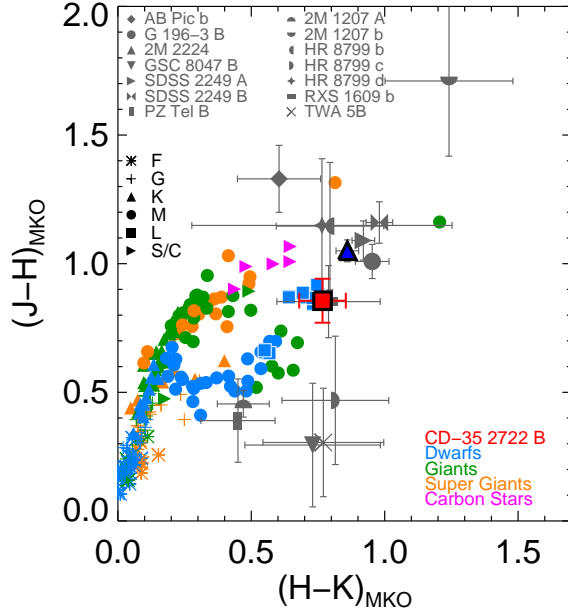


Fig. 6.— The infrared colors of CD-35 2722 B (center red square) plotted along with the colors of field objects and low mass companions. The JHK colors of CD-35 2722 B are consistent with a late-type dwarf, but slightly bluer than that of 2MASS J22244381–0158521 (dark blue triangle), the dusty L4.5 with very similar spectra. The colors also agree completely with those of 1RXS J160929.1–210524 b, which is plotted as a grey rectangle, almost covered by the symbol of CD-35 2722 B. The colors of the field objects are derived from synthesized photometry of published spectra (from Rayner et al. 2009). The L dwarf colors come from the compilation by Leggett et al. (2010) (based on data from Geballe et al. 2002; Golimowski et al. 2004; Knapp et al. 2004; Chiu et al. 2006), with the plotted symbols representing the average color for each L subclass. Also plotted for comparison are the NIR colors for known young late-M and L dwarfs (gray symbols; AB Pic b [Chauvin et al. 2005a], G 196-3 B [Rebolo et al. 1998], 2MASS J22244381–0158521 [Knapp et al. 2004], GSC 8047-0232 B [Chauvin et al. (2005b)], SDSS J053951.99–005902.0 AB [Allers et al. 2010], TWA 5 B [Lowrance et al. 1999], 1RXS J160929.1–210524 b [Lafrenière et al. (2008)], 2MASS 1207334–393254 AB [Mohanty et al. 2007], PZ Tel B [Biller et al. 2010a], HR 8799 bcd [Marois et al. 2008]). Where necessary, color transformations from the 2MASS to the MKO system were made using the Stephens & Leggett (2004) prescriptions for L dwarfs.

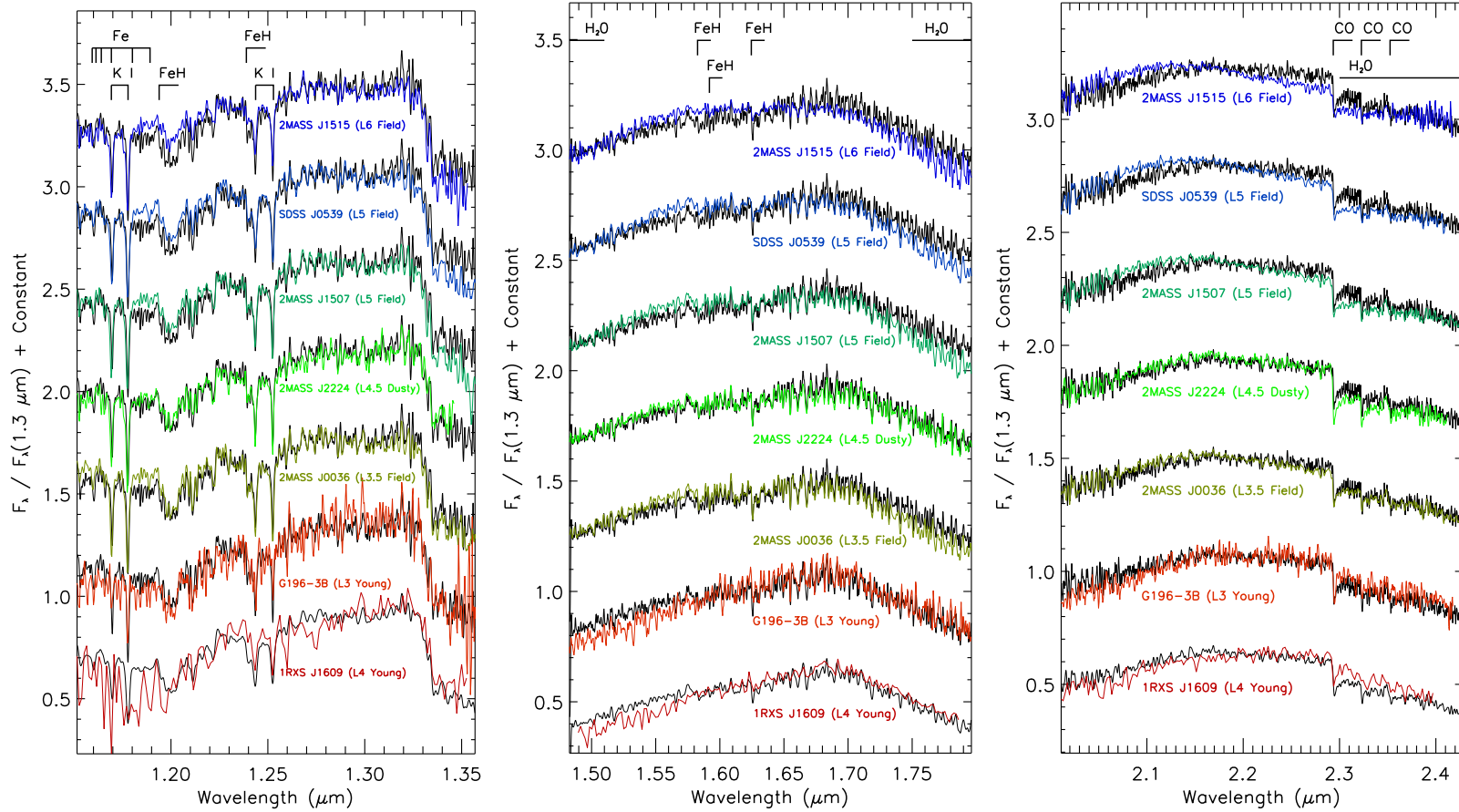


Fig. 7.— Gemini NIFS spectra of CD-35 2722 B (black curves) compared to young (low gravity or dusty) and field L dwarfs. The J , H and K -band spectra are shown in the left, middle and right panels, respectively. The NIFS spectrum is smoothed to match the resolution of the comparison spectra, which have been scaled to fit each band separately. The CD-35 2722 B spectrum is most similar to that of the dusty L4.5 2MASS J22244381-0158521 and the low gravity L3 dwarf G196-3B, and begins to differ significantly from spectra which are more than one subclass away from L4. Thus we assign a spectral type of $L4 \pm 1$ to CD-35 2722 B. The top five comparison spectra (2MASS J15150083+4847416, SDSS J053951.99-005902.0, 2MASS J15074769-1627386, 2MASS J22244381-0158521, 2MASS J00361617+1821104) are from the IRTF spectral library ($R = 2000$; Cushing et al. 2005). The 1RXS J160929.1-210524 b spectra ($R = 850$) are from Lafrenière et al. (2008), while the G196-3 B spectra are from Allers et al. (2010). Molecular features and line identifications are from Cushing et al. (2005).

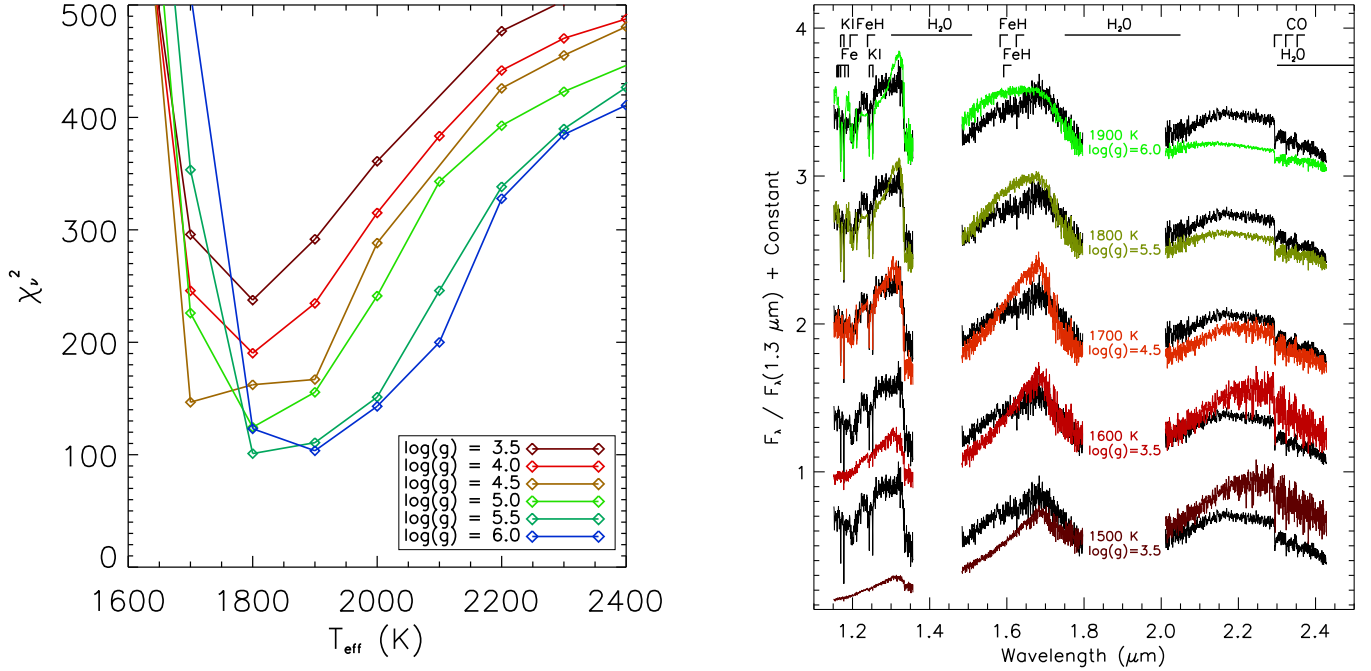


Fig. 8.— Left: The χ^2_ν from fitting Ames-Dusty model atmospheres (Allard et al. 2001) to the NIFS spectra of CD-35 2722 B as a function of model temperature and gravity. The best fit models are the $T_{\text{eff}} = 1700\text{--}1900$ K models with $\log(g) = 4.5\text{--}6.0$ dex. However, none of the models match the continuum shape very well. The reduced chi-squared values quickly deteriorate for $T_{\text{eff}} \leq 1600$ K and $T_{\text{eff}} \geq 2000$ K models. Right: The best fit Ames-Dusty model spectra for different effective temperatures.

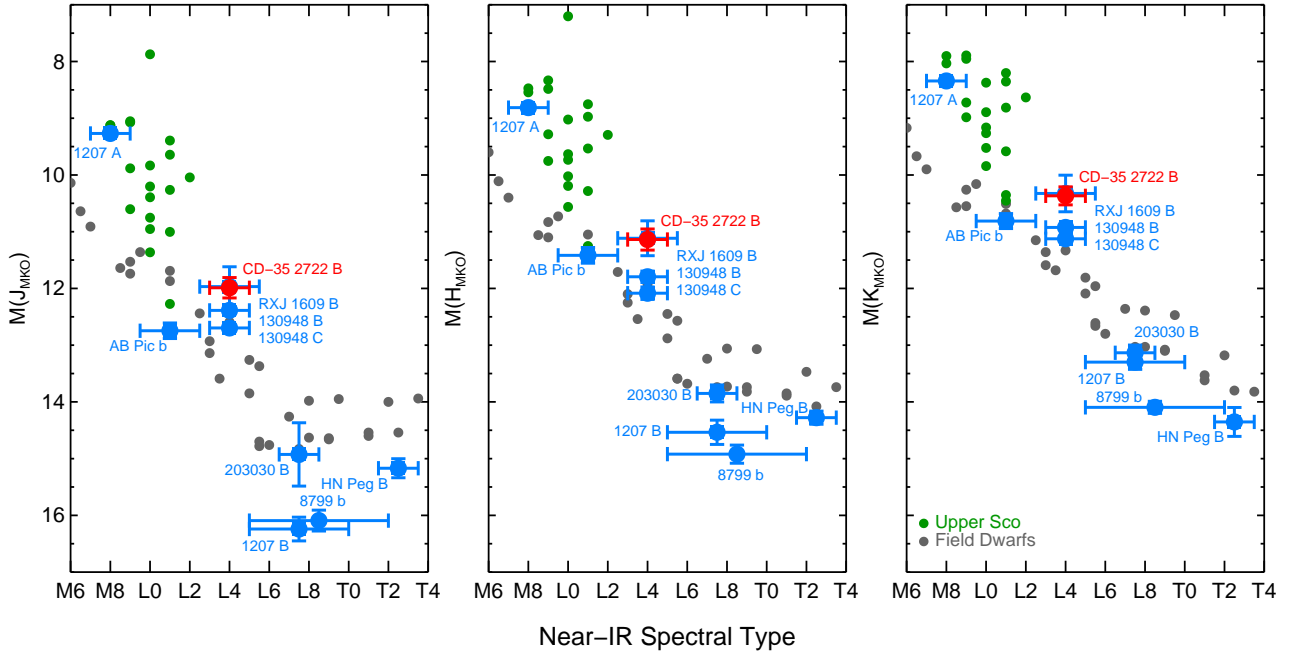


Fig. 9.— The absolute J, H and K MKO magnitudes and spectral type of CD–35 2722 B compared to cool field objects and other young MLT dwarfs with parallax measurements. In the NIR, CD–35 2722 B is over-luminous compared to field objects, but has the same JHK luminosities as the 5 Myr old Upper Sco planet, 1RXS J160929.1–210524 b. Earlier young dwarfs are generally also over-luminous, while later young dwarfs are under-luminous. The objects shown are the MLT dwarf compilation from Leggett et al. (2010) (gray symbols), Upper Sco L dwarfs from Lodieu et al. (2008) (green symbols), 2MASS 1207334–393254 AB (Mohanty et al. 2007), AB Pic b (Chauvin et al. 2005a), 1RXS J160929.1–210524 b (Lafrenière et al. 2008), HD 130948 BC (Dupuy et al. 2009a), HD 203030 B (Metchev & Hillenbrand 2006), HR 8799 b (Marois et al. 2008; Bowler et al. 2010) and HN Peg b (Luhman et al. 2007), all plotted using blue symbols.

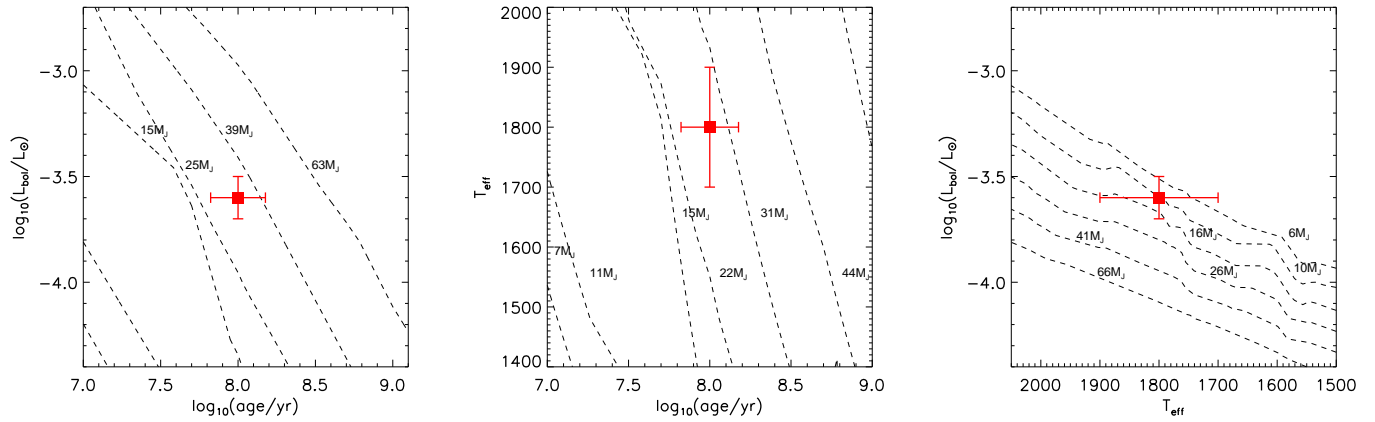


Fig. 10.— Comparison of the properties of CD–35 2722 B to those predicted by the Dusty model mass tracks. The mass estimate derived from the bolometric luminosity and age and from the T_{eff} (derived from model atmosphere fits to the near-IR spectra) and age are consistent with each other.

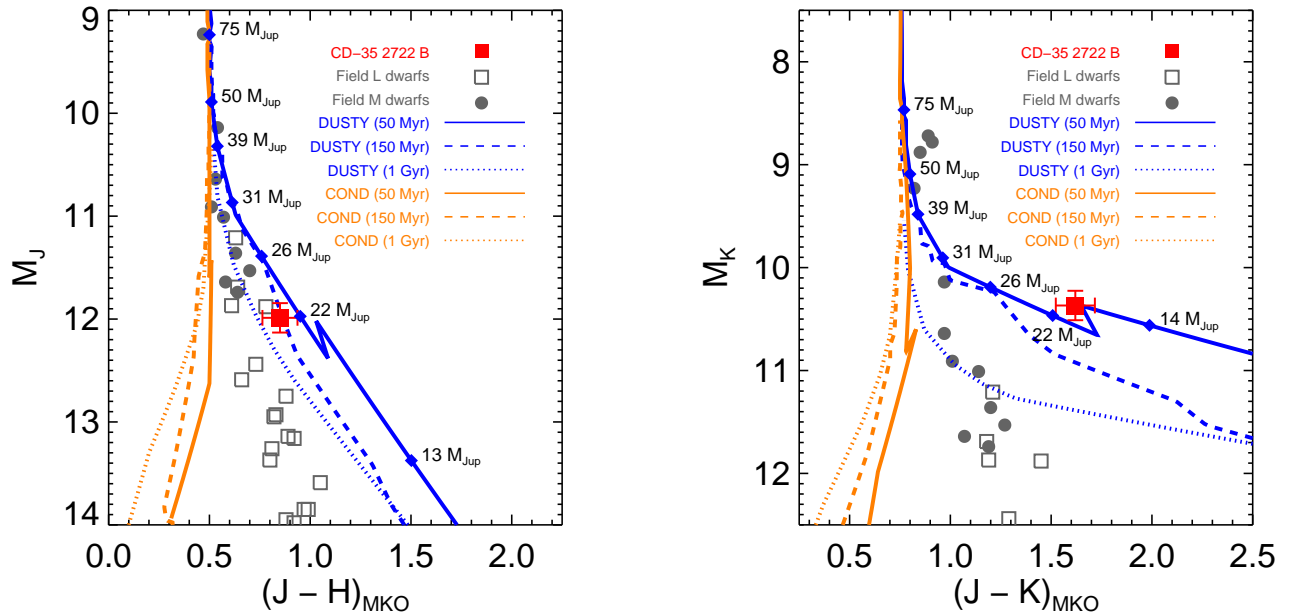


Fig. 11.— Comparison of the COND and Dusty model isochrones at 50 Myr, 150 Myr and 1 Gyr with the absolute magnitudes and NIR colors of CD–35 2722 B shown by the red square. For comparison, we also plot the NIR magnitudes and colors of field M and L dwarfs, from a compilation by Sandy Leggett (Geballe et al. 2002; Goliowski et al. 2004; Knapp et al. 2004; Chiu et al. 2006). As is well known, the COND and Dusty models do not predict the field brown dwarf sequence well at low temperatures.

Table 1. Properties of the CD-35 2722 AB system.

Property	CD-35 2722 A	CD-35 2722 B
Age (Myr) ^a	100±50	
Distance (pc) ^b	21.3±1.4	
Angular separation (") ^c	3.137±0.005	
Physical separation (AU) ^c	67±4	
Position angle (°) ^c	243.10±0.25	
ΔJ , IRTF (mag)	5.77±0.06	
ΔH , IRTF (mag)	5.50±0.06	
ΔK , IRTF (mag)	4.98±0.05	
ΔJ , NICI (mag)	5.66±0.12	
ΔH , NICI (mag)	5.48±0.15	
ΔK_S , NICI (mag)	4.96±0.07	
ΔK , NICI (mag) ^d	4.94±0.07	
J_{MKO} (mag) ^e	7.86±0.03	13.63±0.11
H_{MKO} (mag) ^e	7.28±0.03	12.78±0.12
K_{MKO} (mag) ^e	7.03±0.05	12.01±0.07
M_J (mag)	6.0±0.14	11.99±0.18
M_H (mag)	5.4±0.14	11.14±0.19
M_K (mag)	5.1±0.14	10.37±0.16
$(J - H)_{MKO}$ (mag)	0.58±0.03	0.86±0.13
$(H - K)_{MKO}$ (mag)	0.25±0.02	0.77±0.2
Spectral Type	M1Ve ^f	L4±1
M_{bol} (mag)	8.11±0.25	13.7±0.3 ^g
Mass	0.4±0.05 M_{\odot} ^h	31±8 M_{Jup} ⁱ
T_{eff} (K)	3680±100 ^j	1700–1900 ^k
$\log(g)$ (dex)	...	4.5±0.5 ^l
[Fe/H]	0.04±0.05 dex ^m	...

^aAge estimate for the AB Doradus association (Zuckerman et al. 2004; Luhman et al. 2005; Close et al. 2007).

^bDistance from parallax measurement using CAPScam. See § 3.1 for details.

^cEpoch January 10, 2010 UT.

^dTransformed from NICI ΔK_S magnitude, using the relationship in Stephens & Leggett (2004) and asumming a spectral type of L4.

^eMKO magnitudes derived from 2MASS magnitudes using color transformations in Leggett et al. (2006). All photometry and colors are given in the MKO system. Apparent and absolute magnitudes, colors, and mass estimates for CD-35 2722 B are all derived from IRTF photometry.

^fSpectral Type from Torres et al. (2006).

^gBolometric magnitude of primary derived using bolometric magnitude equations for M dwarfs in Casagrande et al. (2008). Bolometric magnitude for companion derived from M_J , based on bolometric corrections in Liu et al. (2010).

^hMass estimate based on Siess et al. (2000) using M_H and age.

ⁱMass estimate based on Lyon/Dusty model using M_{bol} and age.

^j T_{eff} for an M1V from Gautier et al. (2007)

^k T_{eff} from Ames-Dusty atmospheric model fitting result.

^l Log(g) from fitting Ames-Dusty model atmospheres to the Gemini/NIFS near-IR spectra.

^m[Fe/H] measured by Viana Almeida et al. (2009).

Table 2. Astrometry of objects near CD-35 2722 A.

Object	UT Date (Y/M/D)	Separation (")	Position Angle (°)
CD-35 2722 B	2009/01/06	3.172±0.005	244.13±0.25
	2010/01/10	3.137±0.005	243.10±0.25
background object	2009/01/06	5.312±0.011	275.48±0.25
	2010/01/10	5.316±0.011	276.32±0.25

Table 3. Spectroscopic observations obtained with Gemini-North/NIFS.

UT Date (Y/M/D)	Band	No. of Exp.	Exp. Time(s)	Comments
2010/03/07	<i>J</i>	12	300	
2010/03/18	<i>H</i>	9	300	Partial cloud
	<i>K</i>	4	120	
2010/03/19	<i>J</i>	9	300	Poor conditions, partial cloud

Table 4. Comparison of the sources of uncertainty in CD-35 2722 B's estimated mass.

Parameter	Measurement	Derived Mass Error
Age	100±50 Myr	7 M_{Jup}
Distance	21.3±1.4 pc	0.6 M_{Jup}
Apparent J mag	13.63±0.11 mags	0.3 M_{Jup}
All	...	8 M_{Jup}

Note. — For each parameter, we set the uncertainty in all the other parameters to zero and calculated the error in CD-35 2722 B's mass using the Lyon/Dusty evolutionary models.